R-matrix description of particle energy spectra produced by low-energy ^{3}H+^{3}H reactions

C. R. Brune, J. A. Caggiano, D. B. Sayre, A. D. Bacher, G. M. Hale, and M. W. Paris

Phys. Rev. C **92**, 014003 — Published 20 July 2015

DOI: 10.1103/PhysRevC.92.014003

R-Matrix description of particle energy spectra produced by low-energy T + T reactions

C. R. Brune

Edwards Accelerator Laboratory

Department of Physics and Astronomy

Ohio University, Athens, Ohio 45701, USA

J. A. Caggiano and D. B. Sayre

Lawrence Livermore National Laboratory

Livermore, California 94550, USA

A. D. Bacher

Indiana University Cyclotron Facility (IUCF)

Bloomington, Indiana 47408, USA

G. M. Hale and M. W. Paris

Los Alamos National Laboratory

Los Alamos, New Mexico 87545, USA

(Dated: June 15, 2015)

Abstract

An R-matrix model for three-body final states is presented and applied to a recent measurement of the neutron energy spectrum from the T + T $\rightarrow 2n + \alpha$ reaction. The calculation includes the $n\alpha$ and nn interactions in the final state, angular momentum conservation, antisymmetrization, and the interference between different channels. A good fit to the measured spectrum is obtained, where clear evidence for the ^{5}He ground state is observed. The model is also used to predict the α-particle spectrum from T + T as well as particle spectra from ^{3}He + ^{3}He. The R-matrix approach presented here is very general, and can be adapted to a wide variety of problems with three-body final states.

PACS numbers: 24.10.-i, 24.30.-v, 27.20.+n, 52.57.-z

I. INTRODUCTION

Due to the presence of three particles in the final state, the T + T $\rightarrow 2n + \alpha$ reaction produces distributions of neutron and α-particle energies. The neutron energy spectrum at an effective $E_{c.m.}$ of 16 keV has recently been measured in an inertial confinement fusion experiment at the National Ignition Facility (NIF) [1]. This paper also presented a sequential-decay R-matrix model for the three-body state. The primary purpose of the present paper is to fully describe this model and to explore a broader range of assumptions for the fitting of the neutron spectrum. We also present a prediction for the α-particle spectrum, for which limited data exists. Finally, we calculate the final-state energy spectra of the mirror reaction ^{3}He + ^{3}He and discuss some features of our approach when one of the nuclei in the final state is much heavier than the others.

Our model includes interactions between all pairs of nuclei in the final state. For the T + T case, this implies the $n\alpha$ interaction, including the unbound $3/2^-$ ground and $1/2^-$ first excited state of ^{5}He, and the nn interaction. The calculation also incorporates angular momentum conservation and fermion symmetry. The latter is a particular example of an order-of-emission effect, which give rise to various interference phenomena. In addition, kinematic effects present in the three-body final state are tightly integrated into the model. These details of the model, predictions for particle spectra, and comparisons to available experimental data are discussed below.

The reactions ^{3}He + ^{3}He $\rightarrow 2p + \alpha$ and T + ^{3}He $\rightarrow n + p + \alpha$, which are related by mirror or isospin symmetry to T + T $\rightarrow 2n + \alpha$, are also presently under study at inertial confinement fusion facilities. The model presented here can be adapted to these reactions, and a prediction for the ^{3}He + ^{3}He $\rightarrow 2p + \alpha$ case is given in this paper. This R-matrix approach is very general, and additional areas where it could be applied are discussed in the conclusion.

II. THREE-BODY KINEMATICS

The three-body final state from the T + T $\rightarrow 2n + \alpha$ reaction will be described using non-relativistic kinematics [2]. With the center of mass assumed to be at rest, the kinetic

energy available in the final state is given by

$$E_{tot} = Q + E_{c.m.}, \tag{1}$$

where $Q = 11.332$ MeV and $E_{c.m.}$ is the center-of-mass (c.m.) kinetic energy of the initial state. Here, we will assume $E_{c.m.} = 16$ keV, unless otherwise indicated. The masses of the final-state particles are m_i, where $i = 1$, 2, or 3, and $M = m_1 + m_2 + m_3$. Indices 1 and 2 are used for the neutrons, with index 3 used for the α particle. The momentum and kinetic energies of the final-state particles are given in the three-body c.m. system by $\boldsymbol{p}_i$ and E_i. The relative momentum and kinetic energy of particles i and j are

$$\boldsymbol{p}_{ij} = \frac{\mu_{ij}}{m_i}\boldsymbol{p}_i - \frac{\mu_{ij}}{m_j}\boldsymbol{p}_j \quad \text{and} \tag{2}$$

$$E_{ij} = \frac{p_{ij}^2}{2\mu_{ij}}, \quad \text{where} \tag{3}$$

$$\mu_{ij} = \frac{m_i m_j}{m_i + m_j}. \tag{4}$$

Assuming the indices i, j, and k are all distinct, the relative kinetic energy between particle i and the $j-k$ system is given by $\tilde{E}_i$ and we also have

$$0 = \boldsymbol{p}_1 + \boldsymbol{p}_2 + \boldsymbol{p}_3, \tag{5}$$

$$\tilde{E}_i = \frac{M}{m_j + m_k}E_i, \quad \text{and} \tag{6}$$

$$E_{tot} = E_1 + E_2 + E_3 = \tilde{E}_i + E_{jk}. \tag{7}$$

III. *R*-MATRIX MODEL

The energy distribution of particles emitted by reactions proceeding to unbound states can be described using R-matrix methods, as presented by Barker [3]. This approach in essence describes the particle emissions as sequential two-body decays. Due to the low energy in the initial T + T state, we assume it has orbital angular momentum of zero and thus a total spin and parity of 0^+. We consider here two types of sequential decays: neutron emission to unbound ^{5}He intermediate states and α-particle emission to unbound neutron–neutron states. This latter type decay may also be referred to as di-neutron emission [4]. For both of these decay types, a further complication is presented by the fact that the amplitudes must be constructed to be antisymmetric under the exchange of neutrons, which

give rise to *direct* and *exchange* terms [see Eq. (22) and Eq. (23), respectively]. The R-matrix formalism has been applied to other cases of three-body final states with identical particles in Refs. [5–8].

We emphasize that this approach treats the intermediate state rather carefully. The phase shifts between the particles that make up this state are rather well known for the cases considered here – either experimentally ($n\alpha$ scattering) or theoretically (nn scattering). The R-matrix model described below accurately incorporates these phase shifts. The interaction between the first particle emitted and the intermediate state is, however, not well known, as it generally cannot be studied independently in the laboratory. This part of the matrix element is treated in a minimalist R-matrix approach, with just a hard-sphere interaction, which characterizes a non-resonant phase shift.

A. Neutron emission through ^{5}He intermediate states

For our assumption of a 0^+ initial state, both neutrons must have the identical orbital angular momentum l. We assume the amplitude for the process is given by

$$\mathcal{M}_{\nu_1\nu_2} = \sum_c u_c(\tilde{E}_1) f^{lJ}_{\nu_1\nu_2}(\Omega_1, \Omega_{23}), \tag{8}$$

where ν_i are the spin projections of the neutrons and the energy dependence is described by the R-matrix expression

$$u_c(\tilde{E}_1) = \left[\frac{P_1 P_{23}}{p_1 p_{23}}\right]^{1/2} e^{i(\omega_1-\Phi_1)} e^{i(\omega_{23}-\Phi_{23})} \frac{\sum_\lambda \frac{A_{c\lambda}\gamma_{c\lambda}}{E_{c\lambda}-E_{23}}}{1-[S_{23}-B_c+iP_{23}]R_c} \tag{9}$$

and the spin and angle dependence is given described by $f^{lJ}_{\nu_1\nu_2}(\Omega_1, \Omega_{23})$. The subscripts 1, 2, and 3 refer to the first neutron emitted, second neutron emitted, and the α particle, respectively. The channel is labeled by $c \equiv (l, J, \beta)$, where J is the angular momentum of the intermediate state and β indicates the decay type which is via ^{5}He intermediate states in this case ($\beta = n\alpha$). The quantity R_c is the $n+\alpha$ elastic-scattering R matrix

$$R_c = \sum_\lambda \frac{\gamma^2_{c\lambda}}{E_{c\lambda}-E_{23}} \tag{10}$$

and $E_{c\lambda}$, $\gamma_{c\lambda}$, $A_{c\lambda}$, and B_c are the R-matrix parameters: the level energies, reduced width amplitudes, feeding factors, and boundary-condition constants, respectively. The R-matrix surface functions depend upon the channel radii, l, and energy and include the penetration

factors P_1 and P_{23}, the shift function S_{23}, and the hard-sphere phase shifts $-\Phi_1$ and $-\Phi_{23}$. The quantities ω_1 and ω_{23} are the Coulomb phase shifts which are zero in this case. Note that the penetration factors have been divided by the corresponding momentum. This convention is also used in Refs. [5, 6] and removes two-body phase space factors present in the penetration factors from the three-body matrix element [7]. It should be noted that Eq. (9) is also given in Refs. [5–8], and it is not derived here. As we will show below, this formalism also gives energy distribution formulas consistent with Ref. [3].

The spin and angle dependences are calculated by first coupling a neutron with spin projection ν_2 to an α particle to form a ^{5}He state with angular momentum quantum numbers (J, m_J)

$$g^{lJ}_{\nu_2,m_J}(\Omega_{23}) = \sum_{m,m_l} \langle lm_l \frac{1}{2}\nu_2 | Jm_J - m\rangle Y_{lm_l}(\hat{\boldsymbol{p}}_{23}) \tag{11}$$

and then coupling to another neutron with spin projection ν_1 to form the 0^+ T + T state

$$f^{lJ}_{\nu_1,\nu_2}(\Omega_1,\Omega_{23}) = \sum_{m_J,m,m_l} g^{lJ}_{\nu_2,m_J}(\Omega_{23})\langle Jm_J Jm|00\rangle\langle lm_l \frac{1}{2}\nu_1|Jm\rangle Y_{lm_l}(\hat{\boldsymbol{p}}_1), \tag{12}$$

which can be written

$$f^{lJ}_{\nu_1\nu_2}(\Omega_1,\Omega_{23}) = \sum_{m,m_l,m_l'} \frac{(-1)^{J+m}}{\sqrt{2J+1}}\langle lm_l \frac{1}{2}\nu_1|Jm\rangle\langle lm_l' \frac{1}{2}\nu_2|J-m\rangle Y_{lm_l}(\hat{\boldsymbol{p}}_1)Y_{lm_l'}(\hat{\boldsymbol{p}}_{23}). \tag{13}$$

The quantities in angled brackets are the Clebsch-Gordan coefficients and Y_{lm} are the spherical harmonics with Ω_1 representing the angles (θ_1, ϕ_1) that describe the emission of neutron 1 with momentum $\boldsymbol{p}_1 = p_1\hat{\boldsymbol{p}}_1$ in the three-body c.m. system and Ω_{23} representing (θ_{23}, ϕ_{23}) that describe the the emission of the of neutron 2 in with momentum $\boldsymbol{p}_{23} = p_{23}\hat{\boldsymbol{p}}_{23}$ the rest frame of the $2-3$ system. Finally, our amplitude can be made antisymmetric under the exchange of neutrons by adopting

$$\mathcal{M}_{\nu_1\nu_2} = \sum_c \left[u_c(\tilde{E}_1)f^c_{\nu_1\nu_2}(\Omega_1,\Omega_{23}) - u_c(\tilde{E}_2)f^c_{\nu_2\nu_1}(\Omega_2,\Omega_{13})\right], \tag{14}$$

with Ω_2, Ω_{13}, and related quantities defined analogously to the above.

Our approach only considers $n + \alpha$ configurations for the description of ^{5}He states; this approximation is well justified in this case because the thresholds for other configurations, such as d + T, are located much higher in excitation energy. Below neutron energies of 20 MeV, it is found that considering $l \leq 3$ is sufficient and that one level plus a constant

R^∞ for each channel allows for a good fit to be obtained. We consider here $l = 0$ and 1 transitions involving the $1/2^+$, $1/2^-$, and $3/2^-$ $n + \alpha$ partial waves.

The scattering of neutrons by α particles is very well studied and R-matrix parameters are available [9]. The quality of fit to $n + \alpha$ scattering observables is comparable to modern analyses (e.g., Ref. [10]) that take into account more multichannel data. We utilize the R-matrix parameters given in Table 2 of Ref. [9], with R^∞ replaced by a background level at very high (1000 MeV) excitation energy, which we refer to hereafter to as the R^∞ state. Both $l = 1$ partial waves ($1/2^-$ and $3/2^-$) have a resonant states at low excitation energy, in the range which can be populated by low-energy T+T reactions. Consequently, these partial waves are expected to contribute significantly. Feedings of both the important resonance state and the R^∞ state are considered. We choose the boundary condition constant for these parameters so that the level shift vanishes for the lowest-energy state in each partial wave. The $l = 0$ $1/2^+$ partial wave is non-resonant, but is included due to its low angular momentum. We consider feeding of the $1/2^+$ 50-MeV level (which is in fact a background state), but not the R^∞ state. It should be pointed out that the R^∞ state for this partial wave is unphysical, as it has $\gamma^2_{c\lambda} < 0$. Since this state contributes little to the phase shift in the region of interest, this issue is not a concern for the present work. The channel radius for the $n + \alpha$ parameters is 3.0 fm; for $n + {}^5$He we have used 4.0 fm.

B. Di-neutron emission

We consider here the emission of neutrons in a $l = 0$ spin singlet state, with the orbital angular momentum of the neutron pair with respect to the α-particle core also taken to be zero. In this case we assume the amplitude for the process is given by

$$\mathcal{M}_{\nu_1\nu_2} = u_c(\tilde{E}_3)(f^{0,1/2}_{\nu_1\nu_2} - f^{0,1/2}_{\nu_2\nu_1}), \tag{15}$$

with $c = (0, 1/2, nn)$ for di-neutron emission. The energy dependence is described by the R-matrix expression

$$u_c(E_3) = \left[\frac{P_3 P_{12}}{p_3\, p_{12}}\right]^{1/2} e^{i(\omega_3 - \Phi_3)} e^{i(\omega_{12} - \Phi_{12})} \frac{\frac{A_c\gamma_c}{E_c - E_{12}}}{1 - (S_{12} - B_c + iP_{12})R_c}, \tag{16}$$

where the notation is analogous to that given in the previous section and we also have assumed only a single level such that $R_c = \gamma_c^2/(E_c - E_{12})$. Note also that the shift function

vanishes for $l = 0$ neutrons and we take $B_c = 0$ here. Adopting $E_c = 3.119$ MeV and $\gamma_c^2 = 31.95$ MeV, for a channel radius of 2.0 fm, reproduces the scattering length and effective range of the Argonne V18 potential [11] which are -18.487 fm and 2.840 fm, respectively. In addition, the phase shifts below a neutron energy of 10 MeV are reproduced to within 2.5 degrees with this choice. The $(nn) + \alpha$ channel radius has been taken to be 3.5 fm. The antisymmetric spin singlet state has been generated with the aid of Eq. (13), with $l = 0$ and $J = 1/2$. Note that the there is no angular dependence in this case.

C. Definition of particle energy spectra

Considering both di-neutron emission and the sequential emission of neutrons through ^{5}He states, we arrive at the final form for our matrix element:

$$\mathcal{M}_{\nu_1\nu_2} = \sum_c \left[u_c(12) f^{lJ}_{\nu_1\nu_2}(\Omega_1, \Omega_{23}) - u_c(21) f^{lJ}_{\nu_2\nu_1}(\Omega_2, \Omega_{13}) \right], \tag{17}$$

where the sum is over three $n\alpha$ channels and one nn channel. The nature of the energy dependence of u_c varies with the channel type ($n\alpha$ versus nn); the 12 and 21 notation is used to indicate direct (12) and exchange (21) terms. In principle, all observables can now be calculated. Our primary interest, however, is in calculating the particle energy spectra. The particle distribution in the three-body c.m. system is given by

$$\frac{d^3N}{dE_i\, d\Omega_i\, d\Omega_j} = \sum_{\nu_1,\,\nu_2} |\mathcal{M}_{\nu_1\nu_2}|^2\, p_i p_{jk} \mathcal{J}_{ijk}, \tag{18}$$

where the product of factors $p_i p_{jk} \mathcal{J}_{ijk}$ is the three-body phase space [2, 12], and $\mathcal{J}_{ijk}$ is the Jacobian for the transformation from the $(\tilde{E}_i, \Omega_i, \Omega_{jk})$ system to the $(E_i, \Omega_i, \Omega_j)$ system.

In order to extract the particle energy distributions, it is necessary to integrate out the angular variables. This task can be accomplished most easily by transforming to the $(\tilde{E}_i, \Omega_i, \Omega_{jk})$ system:

$$\frac{dN}{dE_i} = \frac{M}{m_j + m_k} \frac{dN}{d\tilde{E}_i} = \frac{M}{m_j + m_k} \int d\Omega_i\, d\Omega_{jk} \frac{d^3N}{d\tilde{E}_i\, d\Omega_i\, d\Omega_{jk}} \tag{19}$$

$$= \frac{M}{m_j + m_k} \int \frac{d\Omega_i\, d\Omega_{jk}}{\mathcal{J}_{ijk}} \frac{d^3N}{dE_i\, d\Omega_i\, d\Omega_j} \tag{20}$$

$$= \frac{M}{m_j + m_k} \int d\Omega_i\, d\Omega_{jk}\; p_i p_{jk} \sum_{\nu_1,\,\nu_2} |M_{\nu_1\nu_2}|^2 . \tag{21}$$

D. Evaluation of spin and angle-dependent functions

In order to proceed further, it is necessary to evaluate the square of the matrix element, summed over spin projections. In doing so, two types of sums arise:

$$W^{(i)}_{lJl'J'} = (4\pi)^2 \sum_{\nu_1,\,\nu_2} f^{lJ}_{\nu_1\nu_2}(\Omega_i, \Omega_{jk}) f^{l'J'*}_{\nu_1\nu_2}(\Omega_i, \Omega_{jk}) \quad \text{and} \tag{22}$$

$$W^{(12)}_{lJl'J'} = (4\pi)^2 \sum_{\nu_1,\,\nu_2} f^{lJ}_{\nu_1\nu_2}(\Omega_1, \Omega_{23}) f^{l'J'*}_{\nu_2\nu_1}(\Omega_2, \Omega_{13}), \tag{23}$$

where the factors of $(4\pi)^2$ have been inserted for later convenience. The first type of term can be evaluated using standard techniques (see e.g. Ref. [13]):

$$W^{(i)}_{lJl'J'} = [(2J+1)(2J'+1)]^{1/2}(2l+1)(2l'+1) \times \sum_k \langle l0l'0|k0\rangle^2 W^2(klJ'\frac{1}{2}; l'J)(-1)^k P_k(\cos\gamma_{jk}), \tag{24}$$

where the W without subscripts is the Racah coefficient, P_k is the Legendre polynomial of order k, and

$$\cos\gamma_{jk} = \hat{\boldsymbol{p}}_i \cdot \hat{\boldsymbol{p}}_{jk}. \tag{25}$$

The second type of term arises from antisymmetrization and is more complicated to evaluate, due to the fact that, as written, it depends on two sets of angular variables that are not independent. The angular variables are represented by the unit vectors of the momenta. By using Eqs. (2) and (5), $\hat{\boldsymbol{p}}_{23}$ and $\hat{\boldsymbol{p}}_{13}$ can be eliminated using

$$\hat{\boldsymbol{p}}_{23} = \frac{p_2}{p_{23}}\hat{\boldsymbol{p}}_2 + \frac{p_1}{p_{23}}\frac{m_2}{m_2+m_3}\hat{\boldsymbol{p}}_1 \tag{26}$$

$$\hat{\boldsymbol{p}}_{13} = \frac{p_1}{p_{13}}\hat{\boldsymbol{p}}_1 + \frac{p_2}{p_{13}}\frac{m_1}{m_1+m_3}\hat{\boldsymbol{p}}_2 \tag{27}$$

so that the expression only depends on the angular variables $\hat{\boldsymbol{p}}_1$ and $\hat{\boldsymbol{p}}_2$. The spherical harmonics harmonics can then be evaluated for these substitutions using the following addition theorem [14]

$$c^l\, Y_{lm}(\hat{\boldsymbol{c}}) = \sum_{\substack{\lambda_1+\lambda_2=l \\ \nu_1+\nu_2=m}} a^{\lambda_1} b^{\lambda_2} \langle \lambda_1\nu_1\lambda_2\nu_2|lm\rangle \sqrt{\frac{4\pi(2l+1)!}{(2\lambda_1+1)!(2\lambda_2+1)!}} Y_{\lambda_1\nu_1}(\hat{\boldsymbol{a}}) Y_{\lambda_2\nu_2}(\hat{\boldsymbol{b}}), \tag{28}$$

where $\boldsymbol{c} = \boldsymbol{a} + \boldsymbol{b}$ with $\boldsymbol{a} = a\hat{\boldsymbol{a}}$, $\boldsymbol{b} = b\hat{\boldsymbol{b}}$, and $\boldsymbol{c} = c\hat{\boldsymbol{c}}$. The second type of term is then found

TABLE I. The angular functions $W^{(i)}_{lJl'J'}$ given by Eq. (24) and $W^{(12)}_{lJl'J'}$ given by Eq. (29), for the partial wave combinations considered here.

l	J	l'	J'	$W^{(i)}_{lJl'J'}$	$W^{(12)}_{lJl'J'}$
0	$\frac{1}{2}$	0	$\frac{1}{2}$	1	-1
0	$\frac{1}{2}$	1	$\frac{1}{2}$	$-\cos\gamma_{jk}$	$\frac{m_1}{m_1+m_3}\frac{p_2}{p_{13}}+\frac{p_1}{p_{13}}\cos\delta_{12}$
0	$\frac{1}{2}$	1	$\frac{3}{2}$	$-\sqrt{2}\cos\gamma_{jk}$	$\sqrt{2}\left(\frac{m_1}{m_1+m_3}\frac{p_2}{p_{13}}+\frac{p_1}{p_{13}}\cos\delta_{12}\right)$
1	$\frac{1}{2}$	1	$\frac{1}{2}$	1	$-\frac{p_1p_2}{p_{13}p_{23}}\left[\left(\frac{p_2}{p_1}\frac{m_1}{m_1+m_3}+\frac{p_1}{p_2}\frac{m_2}{m_2+m_3}\right)\cos\delta_{12}+1+\frac{m_1m_2}{(m_1+m_3)(m_2+m_3)}\right]$
1	$\frac{1}{2}$	1	$\frac{3}{2}$	$\sqrt{2}P_2(\cos\gamma_{jk})$	$-\sqrt{2}\frac{p_1p_2}{p_{13}p_{23}}\left[\left(\frac{p_2}{p_1}\frac{m_1}{m_1+m_3}+\frac{p_1}{p_2}\frac{m_2}{m_2+m_3}\right)\cos\delta_{12}+P_2(\cos\delta_{12})+\frac{m_1m_2}{(m_1+m_3)(m_2+m_3)}\right]$
1	$\frac{3}{2}$	1	$\frac{3}{2}$	$1+P_2(\cos\gamma_{jk})$	$-\frac{p_1p_2}{p_{13}p_{23}}\left[2\left(\frac{p_2}{p_1}\frac{m_1}{m_1+m_3}+\frac{p_1}{p_2}\frac{m_2}{m_2+m_3}\right)\cos\delta_{12}+1+P_2(\cos\delta_{12})+\frac{2m_1m_2}{(m_1+m_3)(m_2+m_3)}\right]$

to be:

$$
\begin{aligned}
W^{(12)}_{lJl'J'} = (-1)^{J+J'}&[(2J+1)(2J'+1)(2l+1)!(2l'+1)!]^{1/2}(2l+1)(2l'+1)\times \\
&\sum_{\substack{\lambda_1+\lambda_1'=l\\ \lambda_2+\lambda_2'=l'\\ \lambda_3,\lambda_3',\lambda_3'',k}} \left(\frac{p_2}{p_{23}}\right)^{\lambda_1}\left(\frac{m_2}{m_2+m_3}\frac{p_1}{p_{23}}\right)^{\lambda_1'}\left(\frac{p_1}{p_{13}}\right)^{\lambda_2}\left(\frac{m_1}{m_1+m_3}\frac{p_2}{p_{13}}\right)^{\lambda_2'}\times \\
&\left[\frac{(2\lambda_3+1)(2\lambda_3'+1)}{(2\lambda_1)!(2\lambda_1')!(2\lambda_2)!(2\lambda_2')!}\right]^{1/2}(2\lambda_3''+1)\times \\
&\langle\lambda_1 0\lambda_2' 0|\lambda_3 0\rangle\langle\lambda_1' 0\lambda_2 0|\lambda_3' 0\rangle\langle l 0\lambda_3' 0|k 0\rangle\langle l' 0\lambda_3 0|k 0\rangle\times \\
&\begin{Bmatrix}\lambda_1 & \lambda_2' & \lambda_3\\ \lambda_1' & \lambda_2 & \lambda_3'\\ l & l' & \lambda_3''\end{Bmatrix}\begin{Bmatrix}\frac{1}{2} & J & l\\ J' & \frac{1}{2} & l'\\ l' & l & \lambda_3''\end{Bmatrix} W(l'l\lambda_3\lambda_3';\lambda_3''k)(-1)^{\lambda_3'+\lambda_3''-l}P_k(\cos\delta_{12}),
\end{aligned}
\tag{29}
$$

where $\{\}$ indicates the Wigner 9-J symbol and

$$\cos\delta_{12} = \hat{\boldsymbol{p}}_1\cdot\hat{\boldsymbol{p}}_2. \tag{30}$$

The functions $W^{(i)}_{lJl'J'}$ are real and are invariant under the interchange of (l,J) and (l',J'), while $W^{(12)}_{lJl'J'}$ are also real and are invariant under the interchange of (l,J) and (l',J') and particle labels 1 and 2. These functions are tabulated in Table I for the partial wave combinations considered here.

Due to our assumption of a $J=0$ initial state, the particles are emitted isotropically; these functions thus describe the angular correlations between the particles. Note that the particle distribution is a function of two variables, which can be taken to be E_i and $\cos\gamma_{jk}$. From these two quantities, all other needed energies, momentum magnitudes, and angles can be calculated from the kinematics relationships.

E. Calculation of particle energy spectra

We can now write

$$(4\pi)^2 \sum_{\nu_1,\,\nu_2} |\mathcal{M}_{\nu_1\nu_2}|^2 = \sum_{c,c'} g^{(1)}_{cc'} + g^{(2)}_{cc'} + g^{(12)}_{cc'}, \tag{31}$$

where

$$g^{(1)}_{cc'} = u_c(12)\, u^*_{c'}(12)\, W^{(1)}_{lJl'J'}(\cos\gamma_{23}) \tag{32}$$

$$g^{(2)}_{cc'} = u_c(21)\, u^*_{c'}(21)\, W^{(2)}_{lJl'J'}(\cos\gamma_{13}) \tag{33}$$

$$g^{(12)}_{cc'} = -2\,\mathrm{Re}[\, u_c(12)\, u^*_{c'}(21)\,]\, W^{(12)}_{lJl'J'}. \tag{34}$$

If the neutrons were distinguishable, the $g^{(1)}$ contribution would be the neutron 1 distribution and $g^{(2)}$ would be the neutron 2 distribution. The $g^{(12)}$ term arises from treating the neutron as indistinguishable fermions. In the case of neutron emission via intermediate ^{5}He states, we take neutron 1 to the first neutron emitted and neutron 2 to be the second. The neutron energy distribution can be calculated:

$$\frac{dN}{dE_i} = \frac{M}{m_j + m_k}\frac{1}{2}\int_{-1}^{1} d(\cos\gamma_{jk})\, p_i p_{jk} \left[\sum_{c,c'} g^{(1)}_{cc'} + g^{(2)}_{cc'} + g^{(12)}_{cc'}\right] \tag{35}$$

$$= \frac{dN^{(1)}}{dE_i} + \frac{dN^{(2)}}{dE_i} + \frac{dN^{(12)}}{dE_i}. \tag{36}$$

The first term will be called the primary distribution, the second the secondary distribution, and the third the exchange distribution.

If only $n\alpha$ channels are present, the calculation of the primary contribution can be simplified, because u_c then only depends on $\tilde{E}_1$, and $\tilde{E}_1$, p_1, and p_{23} are independent of $\cos\gamma_{23}$. The result is:

$$\frac{dN^{(1)}}{dE_1} = \frac{M}{m_2 + m_3} p_1 p_{23} \sum_c \left| u_c(\tilde{E}_1) \right|^2, \tag{37}$$

which is free from any angular correlation or interference effects. Note also that it is in this situation that the R-matrix energy distribution formula given in Ref. [3] is recovered. For the α-particle energy distribution, all of the contributions must be calculated by numerical integration, but this task is simplified by noting that

$$\frac{dN^{(1)}}{dE_3} = \frac{dN^{(2)}}{dE_3}. \tag{38}$$

If only the nn (di-neutron) channel is present, the calculation also simplifies. In this case we have

$$\frac{dN^{(1)}}{dE_i} = \frac{dN^{(2)}}{dE_i} = \frac{1}{2}\frac{dN^{(12)}}{dE_i}. \tag{39}$$

For the neutron energy distribution, these must be evaluated by numerical integration, but for the α-particle energy distribution we have

$$\frac{dN}{dE_3} = \frac{4M}{m_1 + m_2} p_3 p_{12} \left| u_c(\tilde{E}_3) \right|^2, \tag{40}$$

which is also in the form given by Ref. [3].

In the general case, all three contributions to the distribution must be calculated using numerical integration. We do note that the overall contributions of the primary and secondary distributions are equal, i.e., that

$$\int_0^{\frac{m_j+m_k}{M}E_{tot}} \frac{dN^{(1)}}{dE_i}\, dE_i = \int_0^{\frac{m_j+m_k}{M}E_{tot}} \frac{dN^{(2)}}{dE_i}\, dE_i. \tag{41}$$

1. Spectra for channels in isolation

We will next investigate the nature of the particle energy distributions resulting for each channel in isolation. Note that we make no effort in this section to adjust the feeding factor parameters of the model to fit experimental data; this is done below in Sec. IV. For the $l = 1$ $n\alpha$ channels, we have taken the background feeding to be zero. Each channel thus has only a single feeding factor, which has been adjusted so that $\int \frac{dN}{dE_i} dE_i = 10$. The results are shown in Fig. 1 for the neutron energy distributions and in Fig. 2 for the α-particle energy distributions. For the $n\alpha$ channels, the primary, secondary, exchange, and total contributions are shown for neutron energy distributions, and the primary plus secondary, exchange, and total contributions are shown for the α-particle distributions. For the nn channel, only the total is shown, since, as shown by Eq. (39), the sub-contributions are all proportional. It is interesting to note that the interference introduced by antisymmetrization has a general tendency to be constructive in all cases investigated. This point is discussed further below in Sec. VI.

$1/2^+$ $n\alpha$*:* The particle spectra for this channel are rather featureless. Both the neutron and α-particle spectra closely approximate elliptical energy distributions, characteristic of uniform phase space population.

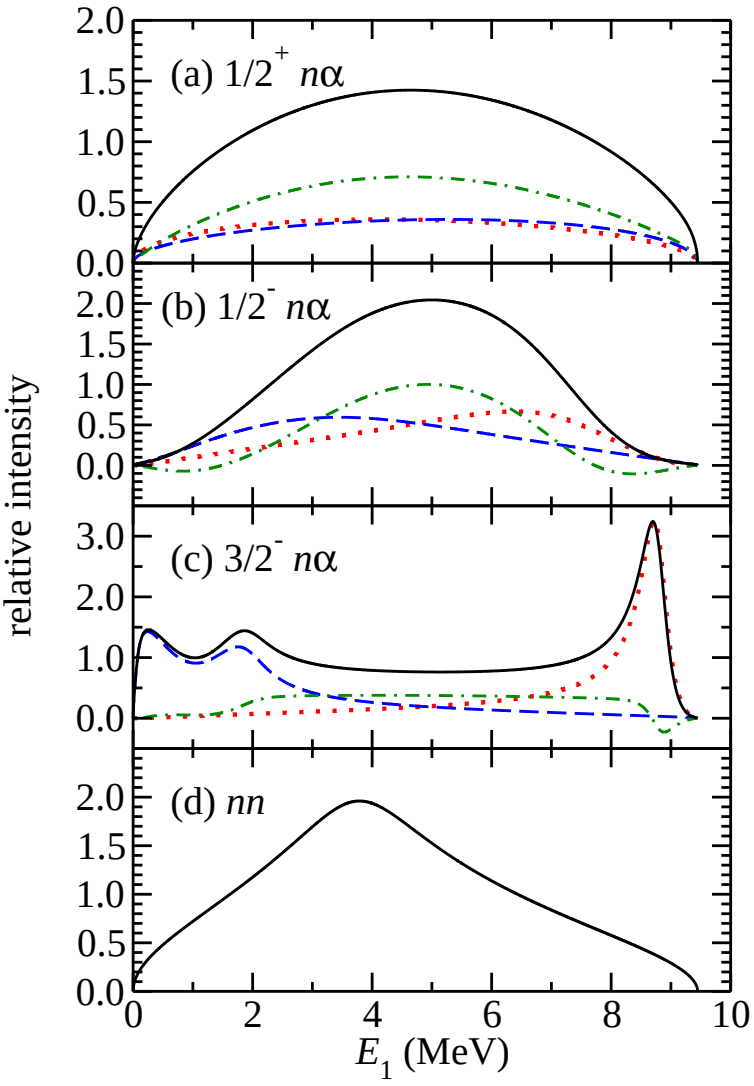

FIG. 1. (Color online) Neutron energy distributions for each channel considered separately. The primary, secondary, exchange, and total are given by the dotted, dashed, dot-dashed, and solid curves, respectively. Only the total is shown for the *nn* case.

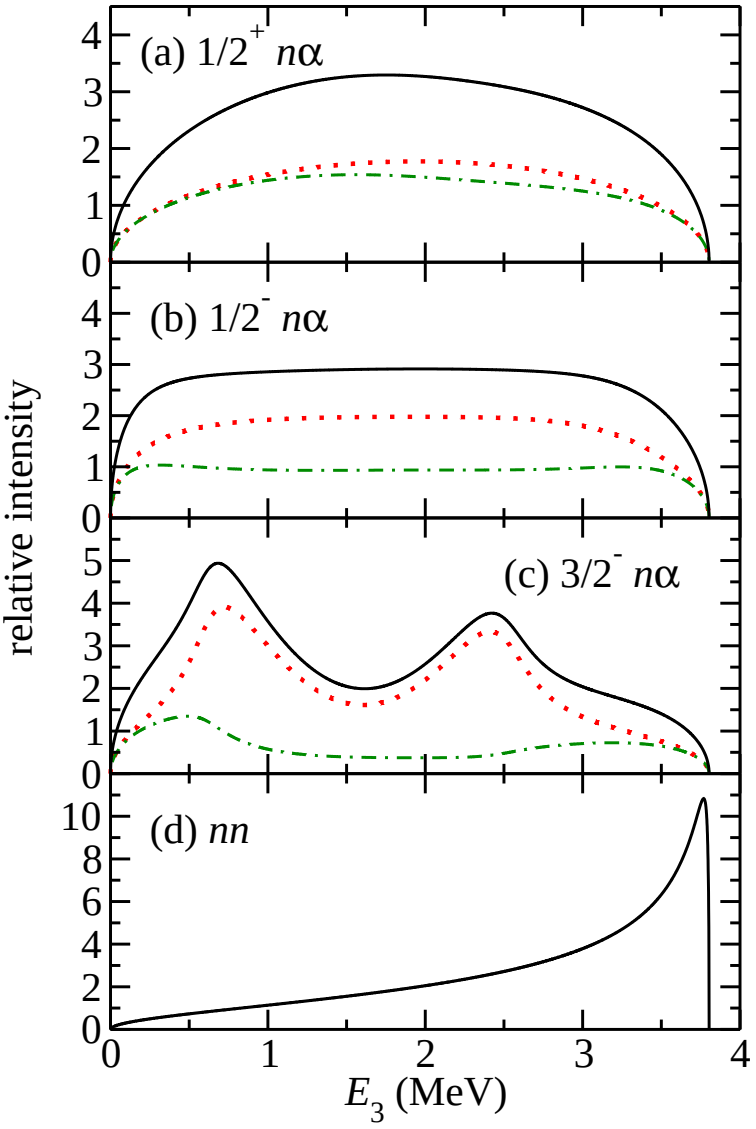

FIG. 2. (Color online) Alpha-particle energy distributions for each channel considered separately. The primary plus secondary, exchange, and total are given by the dotted, dot-dashed, and solid curves, respectively. Only the total is shown for the nn case.

$1/2^-$ $n\alpha$*:* The first excited state of ^{5}He gives rise to a broad peak in the primary neutron spectrum, while the secondary neutron spectrum is also broad, but peaks at a lower neutron energy. The effect of antisymmetrization is to make the overall spectrum narrower, with relatively little strength near the endpoints of the spectrum. The α-particle spectrum for this channel is relatively flat, except near the endpoints.

$3/2^-$ $n\alpha$*:* The ground state of ^{5}He gives rise to a narrow peak in the primary neutron spectrum near the maximum neutron energy. The secondary neutron spectrum shows a double-peaked feature below 2 MeV. This structure results from the $W^{(i)} = 1 + P_2(\cos\gamma_{jk})$ angular correlation between the primary and secondary neutrons, which implies a strong tendency for the neutrons to be emitted in the same or opposite directions, but not perpendicular to each other. Due to the recoil of the ^{5}He intermediate state, this correlation affects the secondary neutron energy distribution. This angular correlation also gives rise to a double peak in the α-particle energy spectrum. These effects on the particle energy spectra due to angular correlations were understood over 50 years ago [15, 16], and were observed for the the α-particle energy spectrum at higher T + T energies [16]. Due to the relatively small energy overlap between primary and secondary spectra, the effect of antisymmetrization on the overall spectra is less important for this channel.

nn*:* In this case, the neutron energy spectrum peaks just below 4 MeV and has considerably less strength near the endpoints compared to the $1/2^+$ $n\alpha$ channel which has the same quantum numbers. The α-particle spectrum has a very distinctive peak near the maximum energy that is associated with the two neutrons being emitted in nearly the same direction with a low relative energy. Similar results for the effect of the nn interaction on the α-particle spectrum were found in the calculations of Lacina, Ingley, and Dorn [4].

2. Interference between channels

Another way to decompose Eq. (35) that is useful when considering multiple channels is

$$\frac{dN}{dE_i} = \sum_c \frac{dN_{cc}}{dE_i} + \sum_{\substack{c,c' \\ c\neq c'}} \frac{dN_{cc'}}{dE_i}, \tag{42}$$

where the second sum is due to interference effects between channels and

$$\frac{dN_{cc'}}{dE_i} = \frac{M}{m_j + m_k}\frac{1}{2}\int_{-1}^{1} d(\cos\gamma_{jk})\, p_i p_{jk} \left[g^{(1)}_{cc'} + g^{(2)}_{cc'} + g^{(12)}_{cc'}\right]. \tag{43}$$

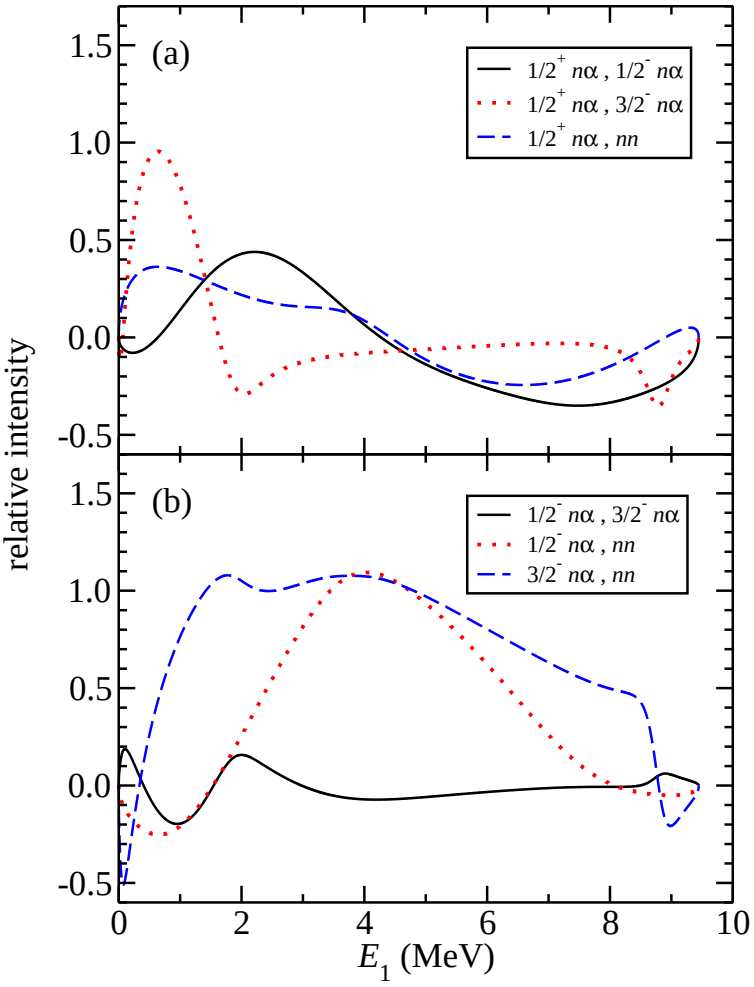

FIG. 3. (Color online) Interference contributions to the neutron energy distributions for partial wave combinations indicated.

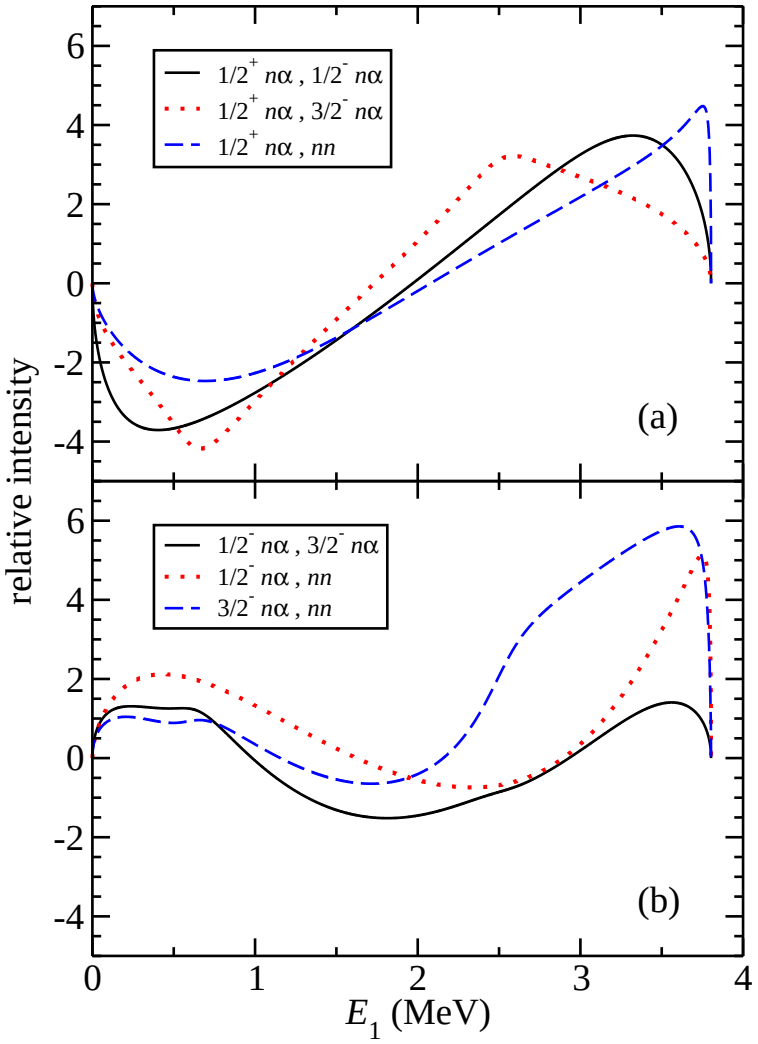

FIG. 4. (Color online) Interference contributions to the α-particle energy distributions for partial wave combinations indicated.

The channel interference contributions to the particle spectra are shown in Figs. 3 and 4, for the partial wave combinations under consideration. The same feeding factors were used as for the calculations shown in Figs. 1 and 2. Note that the signs of the interference contributions are determined by the relative signs of the feeding factors. The effects are seen to be substantial, comparable in magnitude to the single-channel contributions. In addition, note that the contribution of these effects, integrated over E_i, does not vanish.

IV. FITS AND COMPARISONS TO EXPERIMENTAL DATA

In this section, fits and comparisons to experimental neutron and α-particle spectra from low-energy T + T reactions (below $E_{c.m.} = 100$ keV) are presented.

A. Neutron spectrum

The T$(t, 2n)$ neutron spectrum at an effective $E_{c.m.}$ of 16 keV has recently been measured at the NIF [1]. The neutrons were detected in two liquid scintillators along separate lines of sight located 20.1 and 22.2 m from the source, respectively. The experiment provides raw data in the form of digitized currents from the detectors versus time. The data from the 22.2-m detector has been presented in Fig. 2 of Ref. [1], where the time of flight has been converted to a nominal neutron energy and the points have been rebinned. Here we will present additional fits to these data. The fits to the raw data utilize the R-matrix description of the neutron spectrum for $E_{c.m.} = 16$ keV, and take into account the following effects [1]: thermal broadening due to the Maxwell-Boltzmann distribution of particle velocities in the plasma, neutron attenuation and scattering between the T$(t, 2n)$ reaction source and the detector, the light output response of each detector, and the time response of each detector. Finally, the background from the $T(d, n)$ reaction, which was measured separately, was added to the model spectra. The data fitted here are identical to those reported in Ref. [1], except that some additional points at longer times of flight have been included (giving 812 data points in total), and the errors on the data have been increased by assuming that the attenuation correction has a 20% uncertainty and that the scattering correction has a 50% uncertainty. The raw time-of-flight data that are fitted are shown in Fig. 5; note the narrow peak near 500 ns is the peak in the neutron spectrum from the ^{5}He ground state.

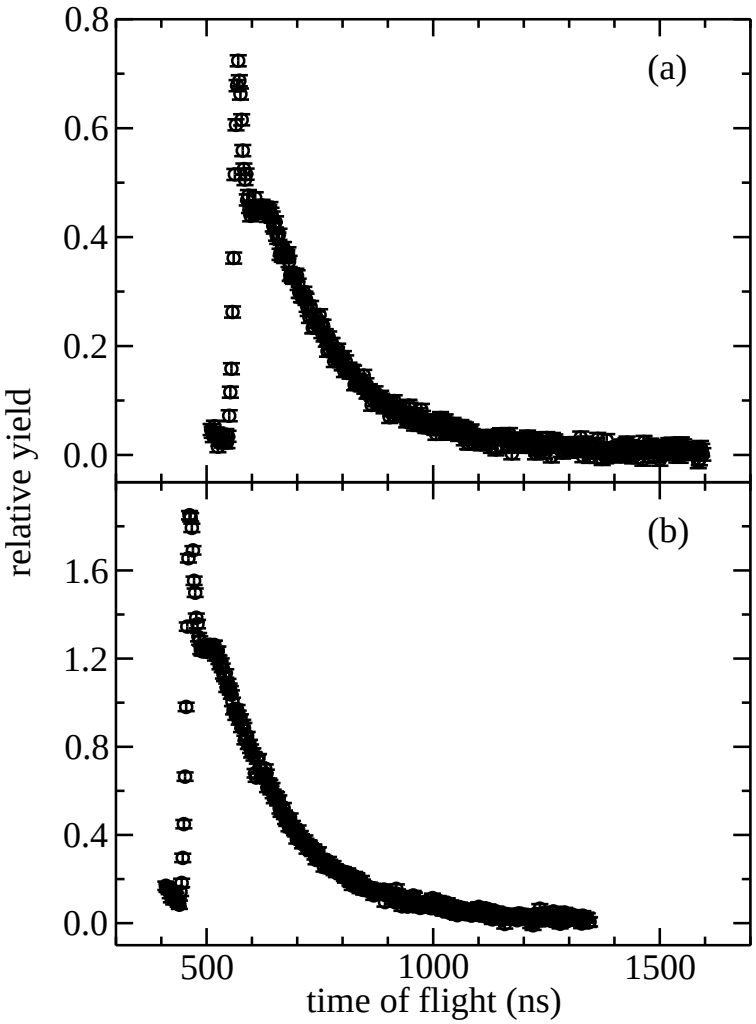

FIG. 5. The neutron time-of-flight spectra from the 22.2-m detector (a) and 20.1-m detector (b) used for fitting.

TABLE II. The $\chi^2_{\rm min}$ values obtained for the various feeding factor assumptions. The presence of a ✓ indicates that a particular feeding factor was varied in the fit; a total of 812 data points were fitted.

fit no.	$n\alpha$					nn	$\chi^2_{\rm min}$
	$1/2^+$	$1/2^-$		$3/2^-$			
	A	A_1	A_2	A_1	A_2	A	
1		✓		✓			2165
2	✓	✓		✓			1316
3		✓		✓		✓	1309
4		✓		✓	✓		1285
5		✓	✓	✓			1095
6	✓	✓		✓		✓	867
7	✓	✓		✓	✓		996
8	✓	✓	✓	✓			660
9		✓	✓	✓	✓		1085
10		✓		✓	✓	✓	920
11		✓	✓	✓		✓	1162
12	✓	✓	✓	✓	✓		659
13	✓	✓		✓	✓	✓	850
14	✓	✓	✓	✓		✓	660
15		✓	✓	✓	✓	✓	667
16	✓	✓	✓	✓	✓	✓	632

The spectra have been fitted using the R-matrix formalism described above, assuming various combinations of the four channels discussed in Sec. III E 1. In addition, we have considered non-zero background feeding factors for the $1/2^-$ and $3/2^-$ $n\alpha$ channels, leading to a total of up 6 variable parameters. Note that the feeding of the low-lying $1/2^-$ and/or $3/2^-$ states in $n\alpha$ channels were always fitted and that if a feeding factor was not fitted, its value has been assumed to be zero. The $\chi^2_{\rm min}$ values obtained for the various feeding factor assumptions are presented in Table II.

Not surprisingly, the $\chi^2_{\rm min}$ decreases steadily as the number of free parameters is increased. In Ref. [1], only the $1/2^-$ and $3/2^-$ $n\alpha$ channels were considered. The fit presented there is nearly identical to fit number 9 presented here, with the very small changes arising from the changes in the data set discussed above. The additional channels are seen to make a substantial increase in the quality of the fit. However, we are cautious about placing a large emphasis on this improvement, as the neutron spectrum data contain neutron-energy-dependent systematic errors from the scattering and attenuation corrections that may be comparable to this improvement in fit (i.e., from $\chi^2_{\rm min} = 1085$ to 632). Two of the fits, numbers 9 and 16, are shown if Fig. 6, where the data have been re-binned and plotted versus the nominal neutron energy.

The R-matrix parameters for fit 16 are shown in Table III. Note that the uncertainties on the feeding factors are computed assuming that uncertainties on the data are random and normally distributed; as explained above this is not strictly the case and the true uncertainties are larger (this is also why some fits are able achieve a χ^2 value which is less than the number of data points). The decomposition of this fit into its various channel components and the net interference contribution, according to Eq. (42), is shown in Fig. 7. It is seen that the fitted $1/2^-$ and $3/2^-$ $n\alpha$ channels, and di-neutron channel, are substantial, with the $1/2^+$ $n\alpha$ channel contributing to a lesser degree. The net interference between channels is also non-negligible. In Ref. [1], a branching ratio for the the $1/2^-$ and $3/2^-$ $n\alpha$ channels was given, which is possible to do if only these two channels are considered, since their interference term is very small. In the general case, it is not possible to determine branching ratios, due to the substantial interference contribution.

In order to facilitate future comparisons with other experiments and calculations, it is desirable to present the neutron spectra in a deconvoluted form, i.e., with the various efficiency, resolution, and background corrections removed. General methods and considerations for

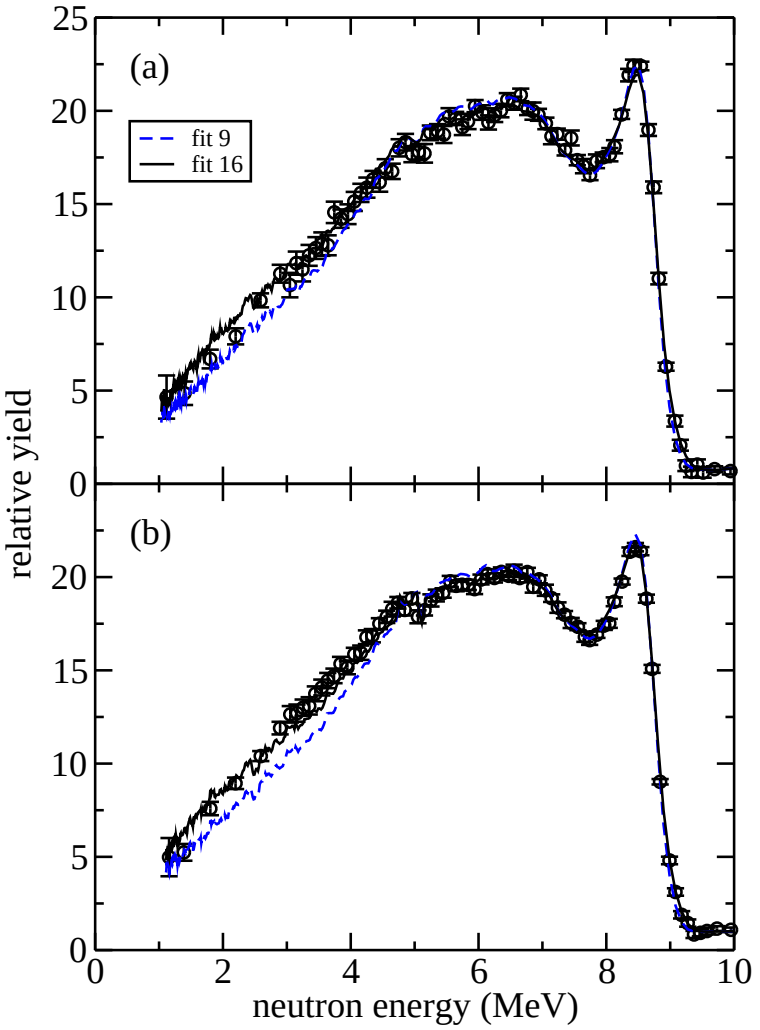

FIG. 6. (Color online) Two fits to the raw neutron spectra, plotted as a function of the nominal neutron energy, for the 22.2-m detector (a) and 20.1-m detector (b). It should be noted that these data, as well as those shown in Fig. 5, still include various experimental factors such as thermal broadening, neutron light output, and detector time response.

TABLE III. The R-matrix parameters for fit 16. Note that the boundary condition parameter is $B = S(E_{c1})$ for the $n\alpha$ channels, and $B = 0$ for the nn channel. The $\gamma_{c\lambda}$ are defined to be the positive square roots of $\gamma^2_{c\lambda}$ and the channel radii are given in Sec. III.

channel	λ	$E_{c\lambda}$ (MeV)	$\gamma^2_{c\lambda}$ (MeV)	$A_{c\lambda}$
$1/2^+$ $n\alpha$	1	50.00	12.00	-18(3)
$1/2^+$ $n\alpha$	2	1000	-40	0
$1/2^-$ $n\alpha$	1	6.43	12.30	-18.2(3)
$1/2^-$ $n\alpha$	2	1000	300	-306(16)
$3/2^-$ $n\alpha$	1	0.97	7.55	9.86(6)
$3/2^-$ $n\alpha$	2	1000	300	155(9)
nn	1	3.119	31.95	12.5(5)

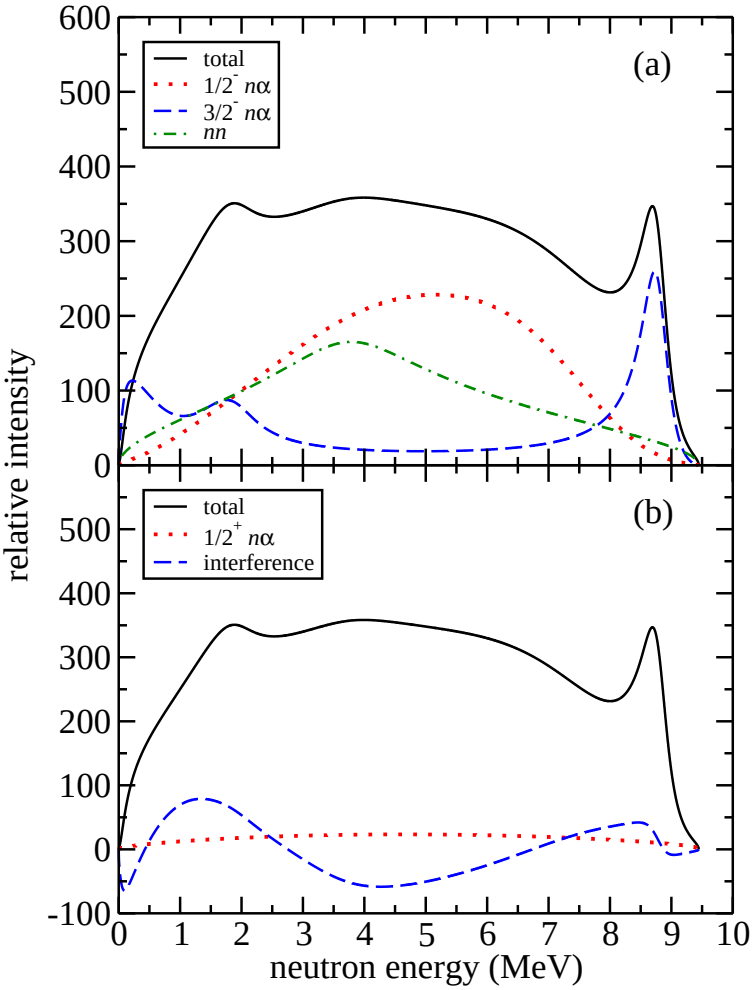

FIG. 7. (Color online) The decomposition of fit 16 into its various channel components and the net interference contribution.

the deconvolution of nuclear science measurements are discussed in Ref. [17]. Any approach to these corrections necessarily involve some model dependence. We have deconvoluted the present measurements by assigning a mean energy to each point (analogous to Eq. (8) of Ref. [17]) and then applying a correction factor to the measured yield for each point (analogous to Eq. (6) of Ref. [17]). This procedure requires that the underlying neutron spectrum be known in advance – for this we use fit 16. In practice, the fit used makes very little difference, as long as it gives a reasonable description of the measured data. The deconvoluted neutron spectrum data is shown in Fig. 8, where the data from the two detectors are combined and re-binned in energy.

B. α-particle spectrum

Some information about the α-particle spectrum from the low-energy T + T reaction is available from a 1985 conference paper by Jarmie and Brown [18], where a measured spectrum and a background spectrum are given for an incident triton energy of 115 keV and a laboratory angle of 45°. We have extracted the α-particle spectrum from their Fig. 8 as follows. The spectrum was first corrected for the background shown along with the spectrum in their figure. Next the spectrum was energy calibrated, using the peak from the $T(d,\alpha)$ reaction to fix the calibration at the high-energy end of the spectrum. The calibration assumed the channel number in the Si detector was linear with α-particle energy with zero offset, with the energy loss in the 30-μg/cm^2 CH_2 foil in front of the detector [19] being taken into account. Finally, the spectrum was converted to the c.m. system assuming the spectrum is isotropic in the c.m. system. It should be noted that this spectrum should be most reliable for the higher energies, where the background is small and the energy calibration is well established. We finally note that this spectrum was measured for $E_{c.m.} = 57.5$ keV, with the beam-energy loss correction being less than 0.1 keV.

The resulting α-particle spectrum, rebinned such that each point represents 5 channels in the raw spectrum, is shown in Fig. 9. Also shown are the predictions from R-matrix fits 9 and 16, where the normalizations of the fits has been adjusted to optimize the agreement with data. It is seen that fit 16 supplies a much better description of the spectrum than fit 9 ($\chi^2 = 46$ versus 140 for the 35 data points). The decomposition of the fit 16 α-particle spectrum into its various channel components and the net interference contribution is shown

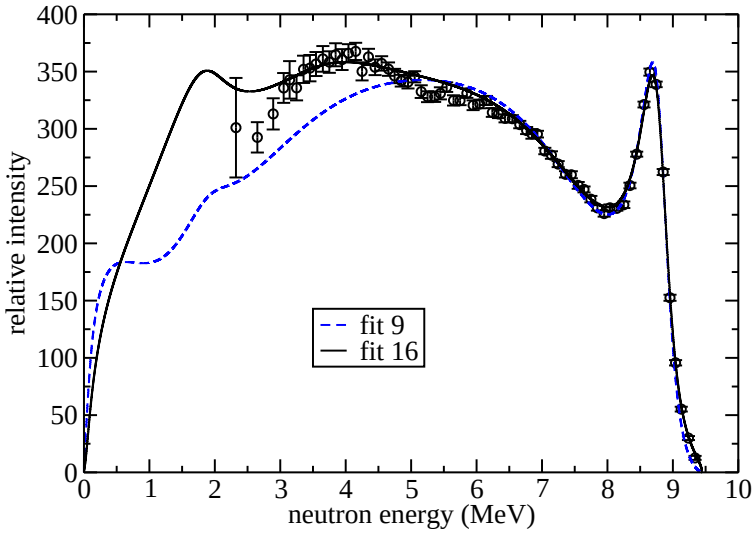

FIG. 8. (Color online) The deconvoluted neutron energy spectrum (points) along with fits 9 and 16 (curves).

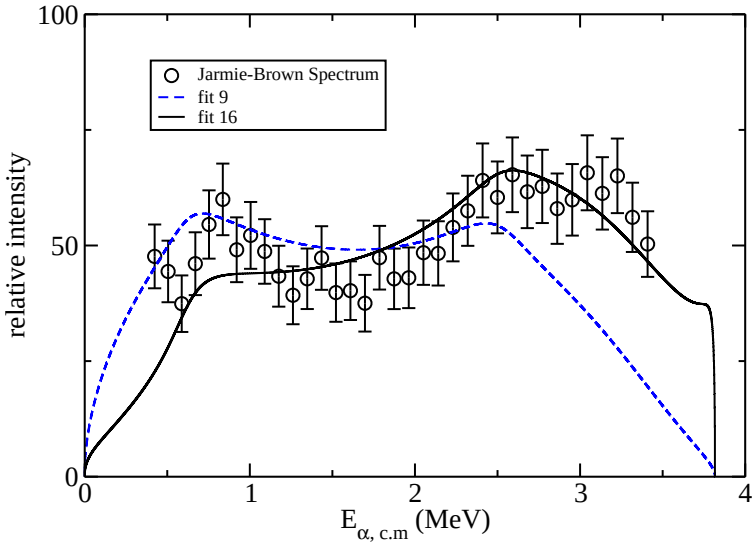

FIG. 9. (Color online) The α-particle spectrum extracted from Ref. [18] (points) and the predictions from fits 9 and 16 (curves).

in Fig. 10. It is seen that the inclusion of the di-neutron channel, which supplies spectral strength near the maximum energy, is crucial for reproducing the spectrum.

C. Dalitz plots

A useful tool for visualizing the the particle energy correlations in a three-body final state is the Dalitz plot. As already noted, the particle distribution given by Eq. (18) is a function of two variables. Taking these to be any pair of particle energies E_i and E_j, we can write

$$\frac{d^2N}{dE_i dE_j} = \frac{M}{2}\left[\sum_{c,c'} g^{(1)}_{cc'} + g^{(2)}_{cc'} + g^{(12)}_{cc'}\right], \tag{44}$$

where the kinematically-allowed region in $E_i - E_j$ space is an ellipse.

The particle distribution resulting from fit 16, plotted as a function of neutron and α-particle energies, is shown in Fig. 11. The vertical band at $E_n \approx 8.7$ MeV and the diagonal band in the lower left part of the ellipse are due to the ^{5}He ground state. The concentration of strength at the top of the ellipse, where $E_\alpha \approx 3.8$ MeV, is due to the di-neutron.

The same particle distribution, plotted as a function of the two neutron energies, is shown in Fig. 12. In this case, the horizontal and vertical bands at $E_n \approx 8.7$ MeV are due to the ^{5}He ground state and the di-neutron strength appears at $E_{n1} \approx E_{n2} \approx 3.8$ MeV.

V. PARTICLE SPECTRA FROM ^{3}He + ^{3}He

It is straightforward to adopt this approach for describing the proton and α-particle spectra from ^{3}He + ^{3}He, which is the mirror reaction to T + T $\rightarrow 2n + \alpha$. For the $p\alpha$ channels, we utilize again the final R-matrix parameters given by Ref. [9], which are defined using the same channel radius and boundary condition conventions as their $n\alpha$ parameters used above. For the pp channel, adopting a channel radius of 2.0 fm, $E_c = 4.865$ MeV, and $\gamma_c^2 = 34.61$ MeV reproduces the scattering length and effective range of the Argonne V18 potential [11] which are -7.8064 fm and 2.788 fm, respectively.

The calculated results for considering each channel in isolation are shown in Figs. 13 and 14. We have assumed $E_{c.m.} = 165$ keV and the same normalization convention was used as for the T + T calculations shown in Figs. 1 and 2. The results are very similar to those found for T + T. The main difference is that the ^{5}Li ground-state peak in $3/2^-$ $p\alpha$

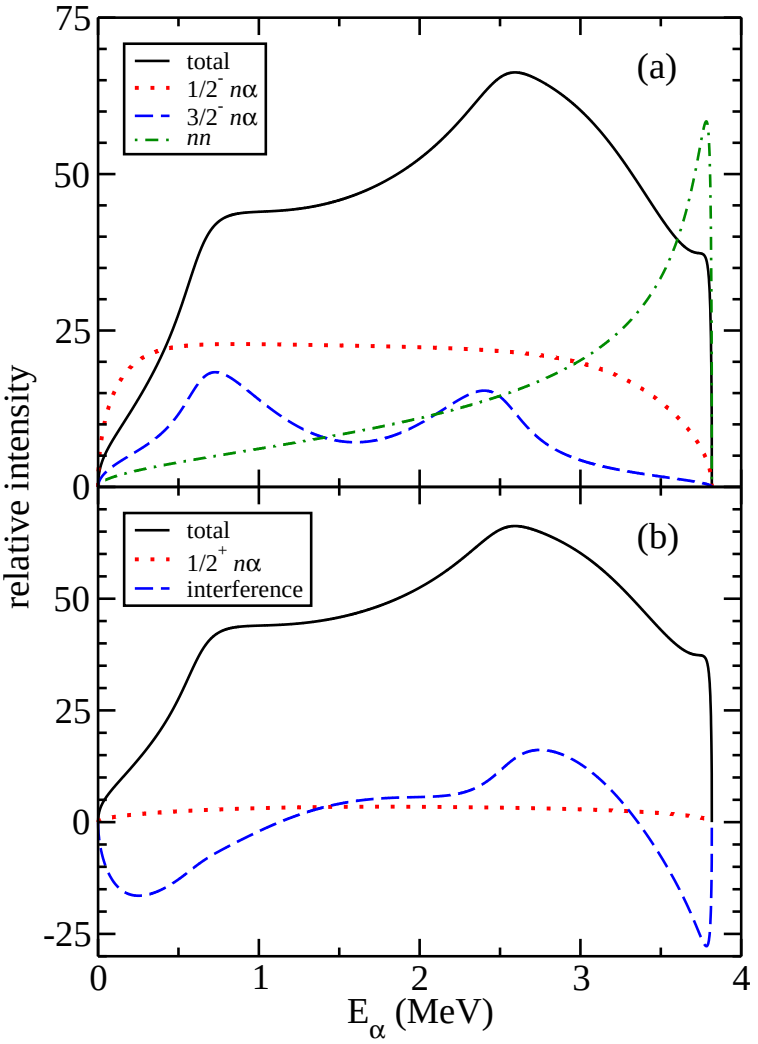

FIG. 10. (Color online) The decomposition of the α-particle spectrum from the fit 16 prediction into its various channel components and the net interference contribution.

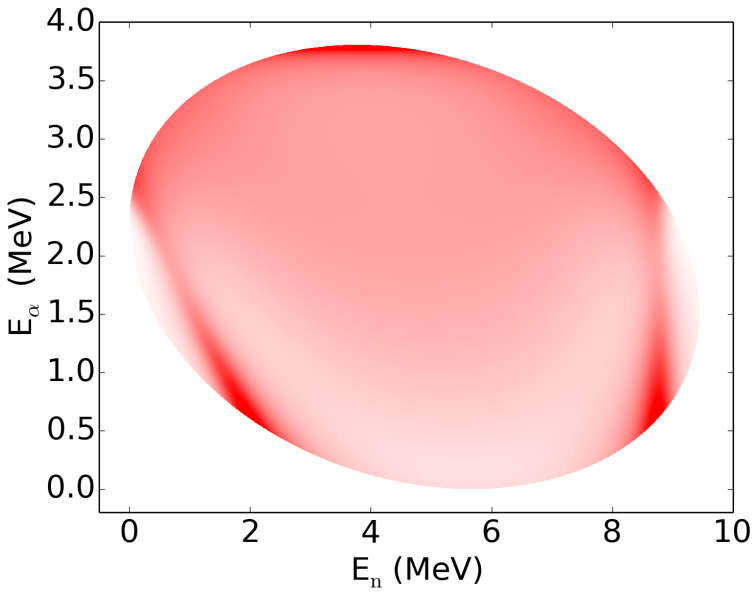

FIG. 11. (Color online) The particle distribution from fit 16 as a function of neutron and α-particle energies.

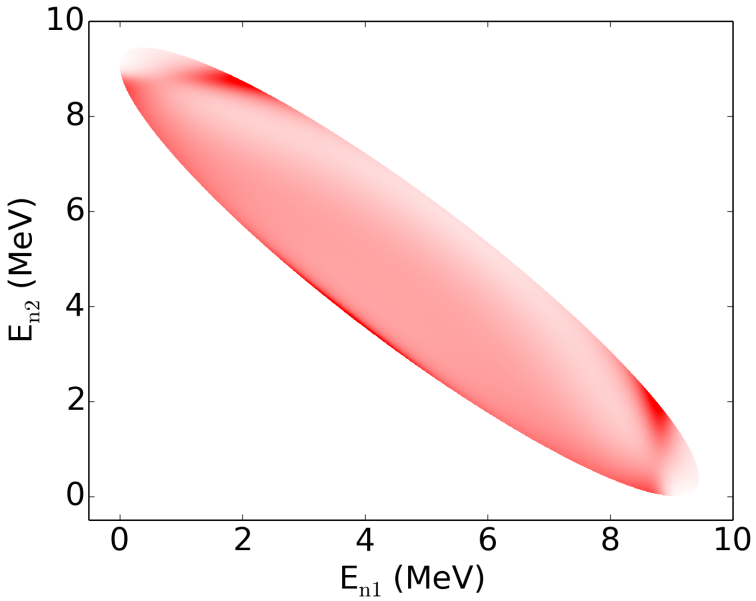

FIG. 12. (Color online) The particle distribution from fit 16 as a function of the two neutron energies.

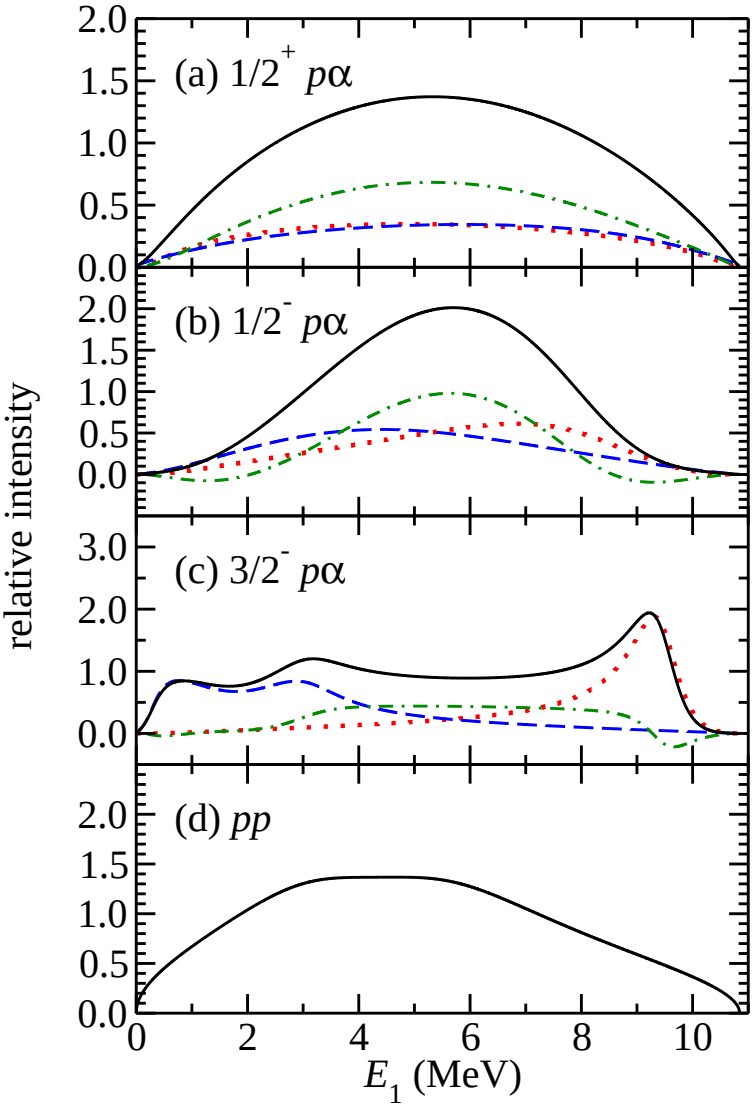

FIG. 13. (Color online) Proton energy distributions from ^{3}He + ^{3}He for each channel considered separately. The primary, secondary, exchange, and total are given by the dotted, dashed, dot-dashed, and solid curves, respectively. Only the total is shown for the *pp* case.

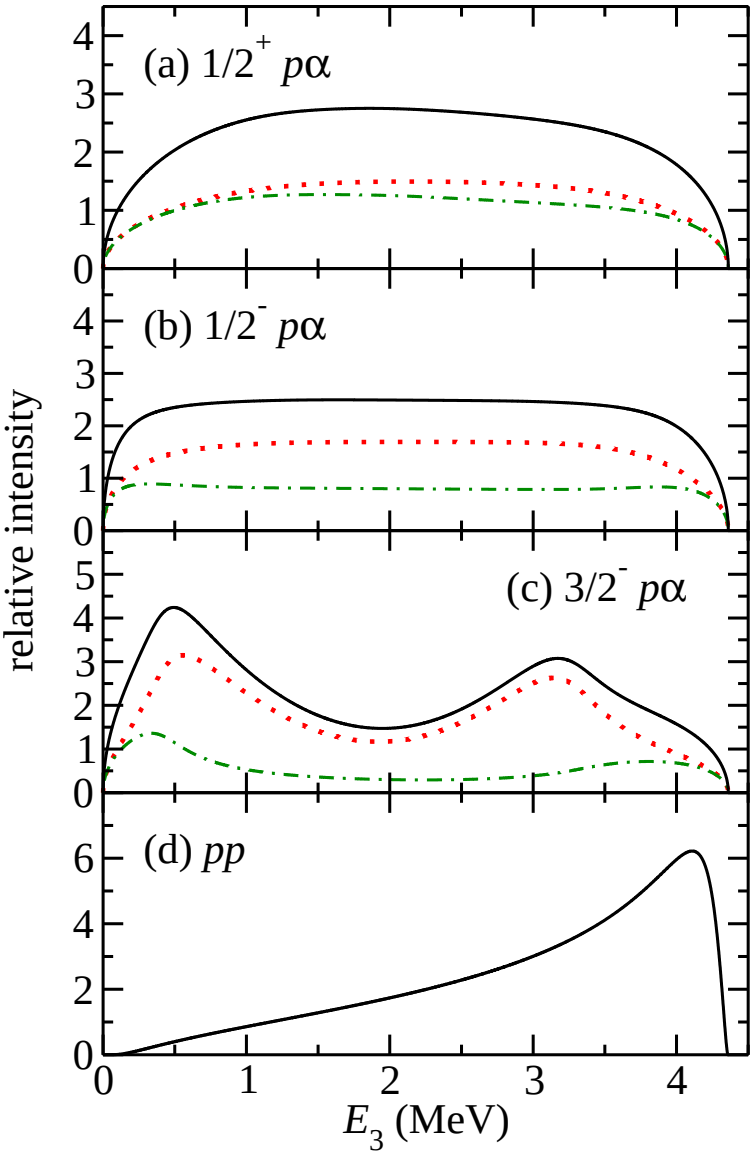

FIG. 14. (Color online) Alpha-particle energy distributions from ^{3}He + ^{3}He for each channel considered separately. The primary plus secondary, exchange, and total are given by the dotted, dot-dashed, and solid curves, respectively. Only the total is shown for the *pp* case.

channel is broader than the ^{5}He peak in the corresponding $n\alpha$ channel, which simply reflects the different intrinsic widths of the states. In addition, the α-particle energy distribution is somewhat broader for the pp channel compared to the corresponding nn channel.

In Fig. 15, we show a prediction for the proton spectrum, where we have assumed the feeding factors from fit 16 to T + T neutron spectrum. The corresponding prediction for the α-particle spectrum is shown in Fig. 16. The main differences from the T + T case are (1) the ^{5}Li ground state is less prominent than the ^{5}He ground state peak in the proton spectrum, due to the former being broader, and (2) there is less strength in the α-particle spectrum near the endpoint (di-proton region), due to the Coulomb barrier between the two protons suppressing the amplitude as their relative energy approaches zero.

It should be noted that we have ignored certain complications introduced by long-ranged Coulomb force to the three-body final state. In particular, our factorized form of the amplitude does *not* correspond to an asymptotic solution to the Schrödinger equation for three charged particles [20, 21]. One can see that our amplitude does not include the effect of the Coulomb barrier as the relative energy goes to zero for *all* particle pairs. For some energy spectra and channels, this deficiency is exposed at the highest energies in the particle spectra, as the endpoint corresponds to the case where the other two particles recoil in the opposite direction with zero relative energy.

An *ad hoc* modification to our amplitudes can be made which restores physically-reasonable behavior near the endpoints. Such an approach may be necessary for describing experimental data in these regions. A simple procedure is to multiply the $p\alpha$ amplitude given by Eq. (9) by $C_{12}C_{13}$ and the pp amplitude given by Eq. (16) by $C_{13}C_{23}$, where

$$C_{ij} = \left[\frac{P_0(k_{ij}a_{ij}, \eta_{ij})}{P_0(k_{ij}a_{ij}, 0)}\right]^{1/2}, \tag{45}$$

and k_{ij}, a_{ij}, and η_{ij} are the wavenumber, channel radius, and Coulomb parameter for particle pair ij. We have assumed $l = 0$ for the penetration factor and used the same radii for the $p\alpha$ and pp channels as discussed above. This modification introduces some additional angular dependence to the matrix element that prevents some of the simplifications based on integrating over Legendre polynomials discussed in Subsec. III E from being applicable. Otherwise, the computations are unchanged. We find that the shapes of the calculated spectra are little changed except near the endpoint while the normalization (area) of the spectra are reduced by 12-17%, depending up on the particular channel. The results with and

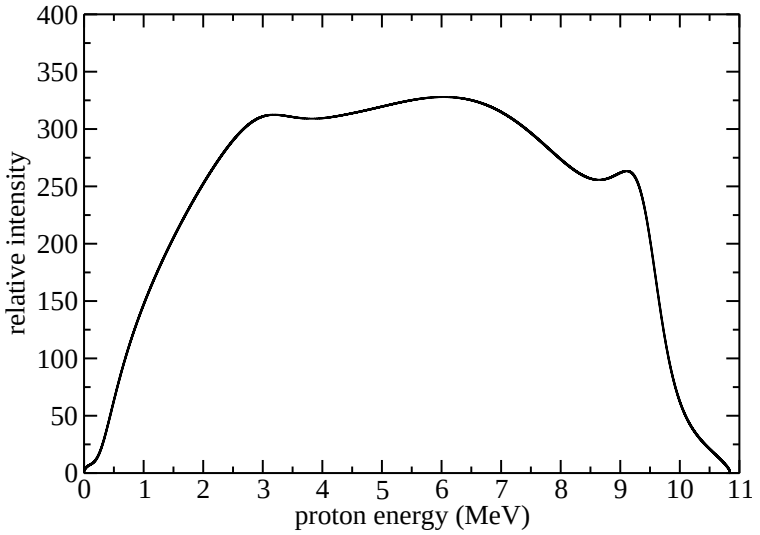

FIG. 15. The predicted $^3\mathrm{He} + {}^3\mathrm{He}$ proton spectrum for $E_{c.m.} = 165$ keV.

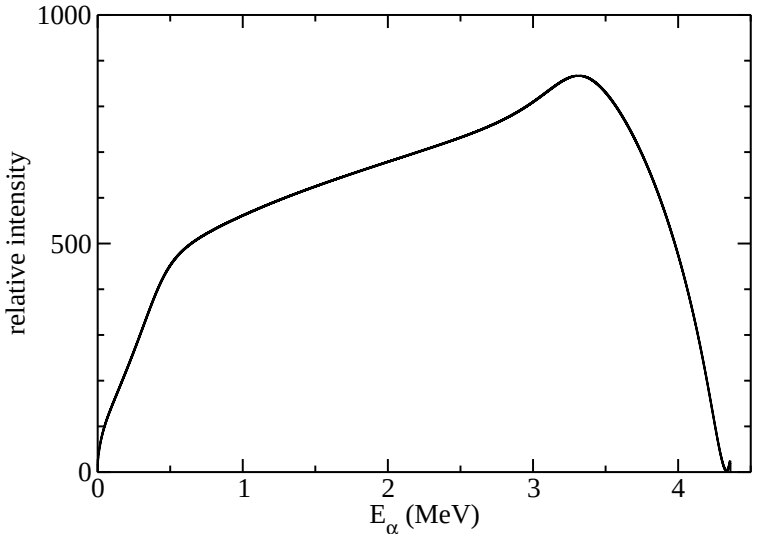

FIG. 16. The predicted $^3\mathrm{He} + {}^3\mathrm{He}$ α-particle spectrum for $E_{c.m.} = 165$ keV.

without this modification are shown in Fig. 17 for the $1/2^+$ $p\alpha$ channel near the endpoint, where the normalization of the modified spectrum was adjusted to match the area of the original spectrum.

VI. HEAVY NUCLEI

It is instructive to consider how this formalism behaves in heavier nuclei. In the limit that $m_3 \gg m_1, m_2$, the kinematic relations simplify considerably. In particular, we have $E_1 + E_2 = E_{tot}$, $p_{23} = p_2$, $p_{13} = p_1$, and $\cos\gamma_{23} = \cos\gamma_{13} = \cos\delta_{12}$. The is also substantial simplification of the angular functions:

$$W^{(1)}_{lJl'J'} = W^{(2)}_{lJl'J'} = -W^{(12)}_{lJl'J'}. \tag{46}$$

If the reaction proceeds via a single channel of sequential light-particle emission, the energy spectrum of light particles is given by

$$\frac{dN}{dE_1} = p_1 p_2 \left| u_c(E_1) + u_c(E_{tot} - E_1) \right|^2, \tag{47}$$

which is symmetric around the center of the spectrum ($E_1 = E_{tot}/2$). Note also that the interference due to antisymmetrization is maximally constructive at the center of the spectrum. This result explains the general tendency observed in Fig. 1 for the antisymmetrization interference contribution to the neutron spectrum to be constructive in the T + T case. This formula was determined using the following special result for the Racah coefficient [13] when $k = 0$

$$W(0lJ'\frac{1}{2}; l'J) = \frac{\delta_{JJ'}\delta_{ll'}}{\sqrt{(2J+1)(2l+1)}}. \tag{48}$$

This result also implies that the interference between channels with distinct l and J values vanishes in this limit.

The interference between channels with distinct l and J values can thus be interpreted to arise via the recoil of the intermediate state. This recoil is substantial in processes involving light nuclei such as $\mathrm{T} + \mathrm{T} \to 2n + \alpha$. In heavier nuclei, the interference between channels is much reduced and is found to scale $\propto 1/m_3$.

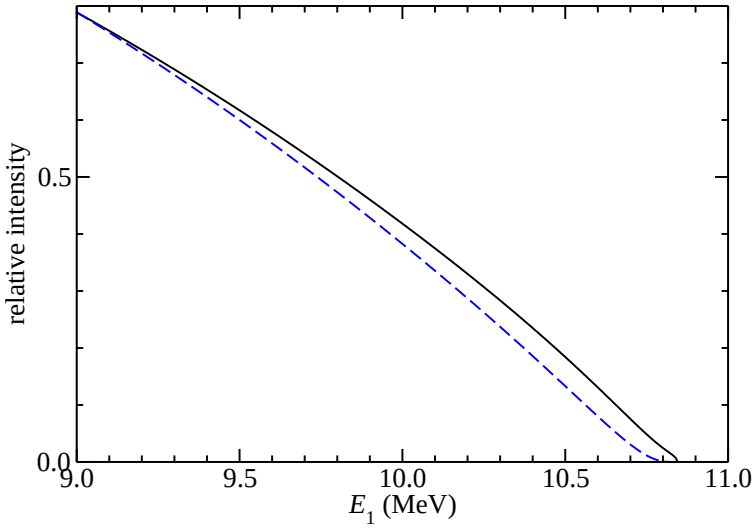

FIG. 17. (Color online) Proton energy distributions from $^3\mathrm{He} + {}^3\mathrm{He}$ for the $1/2^+$ $p\alpha$ channel near the endpoint. The solid curve is the same as shown in Fig. 13 and the dashed curve shows the effect of including the ad-hoc Coulomb correction discussed in the text.

VII. CONCLUSIONS

A phenomenological R-matrix model for the three-body final state of the $\mathrm{T}+\mathrm{T} \rightarrow 2n+\alpha$ reaction has been presented. This approach includes a detailed treatment of the $n\alpha$ and nn interactions in the final state, angular momentum conservation, antisymmetrization, and the interference between different channels. This model is able to supply an excellent fit to the T + T neutron spectrum for $E_{c.m.} = 16$ keV recently measured at the NIF [1]. The most prominent feature in the spectrum is a peak at $E_n \approx 8.7$ MeV, which arises for the $3/2^-$ ^{5}He ground state. The strength in the spectrum at lower neutron energies arises from the $1/2^-$ first excited state of ^{5}He, $1/2^+$ $n\alpha$ emission, and the nn (di-neutron) emission channel. The best fit to the spectrum includes significant strength in the di-neutron channel, but it should be noted that the distribution of strengths in these additional channels is not well constrained by the data (see Table II). This best fit provides a prediction for the α-particle spectrum, which is in reasonable agreement with an experimental spectrum that is available in the literature [18]. The agreement of the prediction with the data near the endpoint of the α-particle spectrum provides support for the significant di-neutron channel strength present in the best fit.

Several issues could be clarified by improved experimental data. It would be very useful to extend the T + T neutron spectrum measurements to lower neutron energies, in order to better constrain the fits and to possibly observe the double-humped structured predicted below 2 MeV neutron energy that is associated with the ^{5}He ground state (see the $3/2^-$ $n\alpha$ panel in Fig. 1). A fully documented measurement of the α-particle spectrum from T + T would also be valuable, particularly if the spectrum could be measured up to the endpoint, where the di-neutron contribution is maximal. It would also be interesting to study the dependence of the spectrum on the energy in the entrance channel, as there is some indication the ^{5}He ground state peak is more prominent at higher entrance channel energies [22].

It is also interesting to consider the reactions $^3\mathrm{He} + {}^3\mathrm{He} \rightarrow 2p + \alpha$ and $\mathrm{T} + {}^3\mathrm{He} \rightarrow n+p+\alpha$, which are related by mirror or isospin symmetry to $\mathrm{T}+\mathrm{T} \rightarrow 2n+\alpha$. A prediction for the proton and α spectra resulting from $^3\mathrm{He} + {}^3\mathrm{He}$ has been given above in Sec. V. Measurements of proton spectra from $^3\mathrm{He} + {}^3\mathrm{He}$ and $\mathrm{T} + {}^3\mathrm{He}$ are currently being pursued with the inertial confinement fusion technique using the OMEGA facility at the Laboratory

for Laser Energetics of the University of Rochester [23].

On the theoretical side, it would be interesting and useful to extend the formalism presented here to include the energy dependence in the initial state. We expect that the methods presented here can be applied to additional reactions or spectra with three-body final states. For example, our approach could be applied to the decay $^{16}\mathrm{Be} \rightarrow 2n + {}^{14}\mathrm{Be}$, where evidence for the di-neutron has been reported [24]. Another area where these methods could be used is the calculation of coherent interference effects between different decay pathways to three-body final states, which has been noted as an important issue for understanding the total widths of states which decay by the emission of three particles [25, 26]. It must also be acknowledged that the phenomenological R-matrix approach presented here includes many approximations. In the future, it is thus hoped that ab-initio techniques based on nucleon-nucleon interactions may be applied to these reactions.

ACKNOWLEDGMENTS

We thank Johan Frenje, Maria Gatu-Johnson, Dennis McNabb, Dieter Schneider, Ian Thompson, and Alex Zylstra for useful discussions. The work was supported in part by the U.S. Department of Energy, under Grant Nos. DE-FG02-88ER40387, DE-NA0001837, and DE-AC52-06NA25396, and by Lawrence Livermore National Laboratory.

---

[1] D. B. Sayre, C. R. Brune, J. A. Caggiano, V. Y. Glebov, R. Hatarik, A. D. Bacher, D. L. Bleuel, D. T. Casey, C. J. Cerjan, M. J. Eckart, R. J. Fortner, J. A. Frenje, S. Friedrich, M. Gatu-Johnson, G. P. Grim, C. Hagmann, J. P. Knauer, J. L. Kline, D. P. McNabb, J. M. McNaney, J. M. Mintz, M. J. Moran, A. Nikroo, T. Phillips, J. E. Pino, B. A. Remington, D. P. Rowley, D. H. Schneider, V. A. Smalyuk, W. Stoeffl, R. E. Tipton, S. V. Weber, and C. B. Yeamans, Phys. Rev. Lett. **111**, 052501 (2013).

[2] G. G. Ohlsen, Nuclear Instruments and Methods **37**, 240 (1965).

[3] F. C. Barker, Australian Journal of Physics **41**, 743 (1988).

[4] B. Lacina, J. Ingley, and D. W. Dorn, *Neutron-neutron interaction in the T+T reaction*, Tech. Rep. UCRL-7769 (Lawrence Radiation Laboratory, 1965).

[5] D. P. Balamuth, R. W. Zurmühle, and S. L. Tabor, Phys. Rev. C **10**, 975 (1974).

[6] D. F. Geesaman, R. L. McGrath, P. M. S. Lesser, P. P. Urone, and B. VerWest, Phys. Rev. C **15**, 1835 (1977).

[7] H. O. U. Fynbo, Y. Prezado, U. C. Bergmann, M. J. G. Borge, P. Dendooven, W. X. Huang, J. Huikari, H. Jeppesen, P. Jones, B. Jonson, M. Meister, G. Nyman, K. Riisager, O. Tengblad, I. S. Vogelius, Y. Wang, L. Weissman, K. W. Rolander, and J. Äystö, Phys. Rev. Lett. **91**, 082502 (2003).

[8] H. O. U. Fynbo, R. Álvarez-Rodríguez, A. S. Jensen, O. S. Kirsebom, D. V. Fedorov, and E. Garrido, Phys. Rev. C **79**, 054009 (2009).

[9] T. Stammbach and R. L. Walter, Nuclear Physics A **180**, 225 (1972).

[10] A. Csótó and G. M. Hale, Phys. Rev. C **55**, 536 (1997).

[11] R. B. Wiringa, V. G. J. Stoks, and R. Schiavilla, Phys. Rev. C **51**, 38 (1995).

[12] J. D. Bronson, Jr., *Three-Alpha Decay of* ^{12}C, Ph.D. thesis, Rice University (1964).

[13] S. Devons and L. J. B. Goldfarb, in *Nuclear Reactions III, Encyclopedia of Physics, Volume 42*, edited by S. Flügge (Springer-Verlag, Berlin, 1957) pp. 362–554.

[14] M. E. Rose, Journal of Mathematics and Physics **37**, 215 (1958).

[15] S. J. Bame and W. T. Leland, Phys. Rev. **106**, 1257 (1957).

[16] N. Jarmie and R. C. Allen, Phys. Rev. **111**, 1121 (1958).

[17] C. R. Brune and D. B. Sayre, Nuclear Instruments and Methods in Physics Research Section A: Accelerators, Spectrometers, Detectors and Associated Equipment **698**, 49 (2013).

[18] N. Jarmie and R. E. Brown, Nuclear Instruments and Methods in Physics Research Section B: Beam Interactions with Materials and Atoms **10/11**, 405 (1985).

[19] N. Jarmie, R. E. Brown, and R. A. Hardekopf, Phys. Rev. C **29**, 2031 (1984).

[20] E. O. Alt and A. M. Mukhamedzhanov, Phys. Rev. A **47**, 2004 (1993).

[21] A. M. Mukhamedzhanov and M. Lieber, Phys. Rev. A **54**, 3078 (1996).

[22] C. Wong, J. D. Anderson, and J. W. McClure, Nuclear Physics **71**, 106 (1965).

[23] A.B. Zylstra (unpublished).

[24] A. Spyrou, Z. Kohley, T. Baumann, D. Bazin, B. A. Brown, G. Christian, P. A. DeYoung, J. E. Finck, N. Frank, E. Lunderberg, S. Mosby, W. A. Peters, A. Schiller, J. K. Smith, J. Snyder, M. J. Strongman, M. Thoennessen, and A. Volya, Phys. Rev. Lett. **108**, 102501 (2012).

[25] F. C. Barker, Phys. Rev. C **68**, 054602 (2003).

[26] A. J. Bartlett, J. A. Tostevin, and I. J. Thompson, Phys. Rev. C **78**, 054603 (2008).